NANOTECHNOLOGY, NANOPOLLUTION, NANOTOXICOLOGY AND NANOMEDICINE (NNNN)

CrossMark

Improving of the Mg-Co nanoferrites efficiency for crude oil adsorption from aqueous solution by blending them with chitosan hydrogel

Zizi I. Abdeen[1] · Amina I. Ghoneim[2]

Abstract

The efficiency of the as-prepared $Mg_{0.25}Co_{0.75}Fe_2O_4$ spinel nanoparticles for adsorption of crude oil from aqueous solution was improved by blending them with chitosan hydrogel (CH) prepared using epichlorohydrin as cross-linker resulting (CH/$Mg_{0.25}Co_{0.75}Fe_2O_4$) nanocomposites. $Mg_{0.25}Co_{0.75}Fe_2O_4$ nanocrystals was prepared by the chemical co-precipitation method and characterized by using X-ray diffraction (XRD), infrared spectroscopy (FT-IR), scanning electron microscope (SEM), transmission electron microscope (TEM), and differential thermal analysis (DTA)/thermogravimetric analysis (TGA). DTA/TGA results showed that the net weight loss of the samples heated from room temperature up to 1000 °C lies in the range 2.2–26.5% weight, where the maximum weight loss appeared at 100 °C and 614 °C. The blending nanocomposites prepared, were characterized by FT-IR and SEM micrographs. The effect of the nanoparticles ratio on the water uptake of nanocomposites and their capability to adsorb the crude oil was estimated by the gravimetric method. TEM results showed that the average nanoparticle size (Z) of $Mg_{0.25}Co_{0.75}Fe_2O_4$ is 30.06 nm and the SEM illustrated the presence of a very clear and rough layer of pores which are homogenously arranged structures that could play an important role in the adsorption and stability of crude oil on polymers. The adsorption ability of crude oil from waste water on the CH/$Mg_{0.25}Co_{0.75}Fe_2O_4$ nanocomposites hydrogel was reported and it was found that the CH/$Mg_{0.25}Co_{0.75}Fe_2O_4$ with 95/5% ratio showed the improvement in the oil adsorption (72.5%) than the 0/100% one (50.2%). As a consequence, it is highly suggested that the potential of blending CH with $Mg_{0.25}Co_{0.75}Fe_2O_4$ to obtain CH/$Mg_{0.25}Co_{0.75}Fe2O_4$ for enhancing crude oil adsorption in oily waste water treatment with a low cost.

Keywords $Mg_{0.25}Co_{0.75}Fe_2O_4$ nanoparticles · CH/$Mg_{0.25}Co_{0.75}Fe_2O_4$ nanocomposites · Hydrogel · Structural properties · Water treatment

Introduction

Recently, the plurality of researchers are concerning with synthesizing new nanomaterials with unique chemical, structural, spectral, and thermal attributes, in order to promote and contribute to the ongoing progression of the newly enhanced modern industrial technologies and approaches (Kefeni et al. 2017; Jagadeesha et al. 2016; Paramesh et al. 2017; Akhtar et al. 2018; Yadav et al. 2016), aiming to make the human life much better and have brighter future. One of the so intelligent and good materials is nanoferrites. Nanoferrites are iron containing complex oxide materials, having the general formula MFe_2O_4, where M is divalent metal cation like Co^{2+}, Mg^{2+}, and Zn^{2+} (Goldman 2006; Amer et al. 2015). Variation of doping cations in these nanocrystalline materials alters their structural, spectral, thermal, physical, and chemical merits. Therefore, synthesizing nanocrystalline cobalt ferrites with their particular physical and chemical characteristics gives prominence for using these versatile nanostructured materials as important candidates for abundant fields and numerous technological applications including; communication technology, nanodrug delivery, biosensors, MRI, MW absorbers and devices, gas sensation, permanent magnets, and enhanced water treatment (Thakur et al. 2016).

✉ Amina I. Ghoneim
mona_ghoneim@yahoo.com

[1] Petrochemicals Department, Egyptian Petroleum Research Institute, Cairo, Egypt

[2] Physics Department, Faculty of Science, Tanta University, Tanta, Egypt

⚛ Springer

The needing to clean up water is the most importante issue and distinctly is the obvious universal menace for human-kind and other living creatures all over the world. Distinctly, contaminated water, which have many provenances such as industrial enterprise residues and human wastefulness and junk, is presumed to be a prevalence and essential pollutant source, at which these deleterious pollutants ultimately lead to reducing water quality and nature. Therefore, water reuse is a very challenging issue, which requires smart synthesized nanostructured materials, e.g., spinels (magnetic semiconductors) with electrical and magnetic significant attributes and also their considerable surface area (Attia et al. 2017). Oil waste is adsorbed using natural adsorbents, for instance, bentonite organically (Panpanit and Visvanathan 2001), peat (Sharma et al. 2015), and activated carbon (Inagaki et al. 2002). Owing to the elevated cost and diminished adequacy of activated carbon for treatment of wastewater oil (Ibrahim et al. 2010), the preference of using low-cost materials as substituted one was early investigated (Moazedh 2005, Abdeen and Moustafa 2015). The structures of polymeric hydrogels are matrixes with cross-linked three-dimensional forming hydrophilic homopolymers or copolymers (Abdeen 2005, 2011; Abdeen et al. 2015, 2017). It can swell rapidly in the aqueous solution as a result of its super hydrophilicity characteristics, which is useful for shortening the time to reach the adsorption equilibrium (Kasgöz et al. 2008).
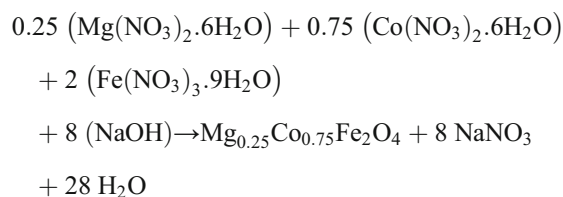
For exploring various features and properties of the spinel $Mg_{0.25}Co_{0.75}Fe_2O_4$ nanoparticles, which have been obtained using the facile one-pot synthesis strategy through the eco-friendly co-precipitation route, some physical analyses have been done using XRD, FT-IR, TEM, SEM, and thermal investigations using thermogravimetric analysis (TGA) and differential thermal analysis (DTA). Furthermore, CH/$Mg_{0.25}Co_{0.75}Fe_2O_4$ blending hydrogels were prepared by blending method using epichlorohydrin (Abdeen et al. 2017) as cross-linker CH/$Mg_{0.25}Co_{0.75}Fe_2O_4$ was prepared and based on $Mg_{0.25}Co_{0.75}Fe_2O_4$ to uniquely fabricate a smart magnetic nanocomposite. Epichlorohydrin was then used as a chemical cross-linking agent to form network structures as well as to improve the hydrogel stability. The efficiency of $Mg_{0.25}Co_{0.75}Fe_2O_4$ and CH/$Mg_{0.25}Co_{0.75}Fe_2O_4$ nanocomposite hydrogel to adsorb oil from waste water was evaluated. As well, these marvelous and new nanocomposites were extensively investigated using XRD, FT-IR, and SEM.

Experimental techniques

Preparation of $Mg_{0.25}Co_{0.75}Fe_2O_4$ nanoparticles

The as-prepared $Mg_{0.25}Co_{0.75}Fe_2O_4$ spinel nanoparticles have been fabricated using the facile one-pot synthesis strategy

through the eco-friendly co-precipitation route according to the following equation (Amer et al. 2014):

$$0.25\left(Mg(NO_3)_2.6H_2O\right) + 0.75\left(Co(NO_3)_2.6H_2O\right)$$

$$+ 2\left(Fe(NO_3)_3.9H_2O\right)$$

$$+ 8\,(NaOH) \rightarrow Mg_{0.25}Co_{0.75}Fe_2O_4 + 8\,NaNO_3$$

$$+ 28\,H_2O$$

Stoichiometric amounts of $Mg(NO_3)_2.6H_2O$, $Co(NO_3)_2.6H_2O$, and $Fe(NO_3)_3.9H_2O$ were dissolved in distilled water and kept at 10 °C for 1 h. Metal nitrates were persistently stirred using a variable magnetic stirrer. The pH value of the mixed nitrate solution was permanently monitored as NaOH concentrated solution was added drop-by-drop until pH value equal 12. Then, the well-mixed solution was heated up to 80 °C for 2 h in synchrony with the persistent mixing. The ultrafine precipitates were entirely washed with distilled H_2O until the washings become free from NaCl. The fine precipitates were dried at room temperature. Then, the ultrafine dried precipitates were finely ground in a cleaned agate mortar to obtain the nanopowder (Amer et al. 2014).

Preparation of chitosan

The chitinous material (shells of the shrimp) was decalcificated with 1.0 M HCl (3.0% w/v) at room temperature with constant stirring for 1.5 h. The decalcified product was filtrated, washed, and dried, then deproteinized with 4% NaOH solution at 50 °C with constant stirring for 5 h. The deproteinized chitin has been filtered and carefully washed with deionized distilled H_2O until the pH became neutral. It was dried up twice with Ch_3OH, and one more time with C_3H_6O, and then completely dried. The well-dried chitin was added to boiling 0.1% $KMnO_4$ solution in order to eliminate the odious scent and it has been mixed with 15% $C_2H_2O_4$ solution aiming to dispose of the appearing color. Thus, the essential steps start with the filtration of the produced chitin, then washing it with distilled H_2O and finally drying it. The chitosan was ultimately obtained by putting the well-dried chitin into a three-necked flask containing a solution of 40% (w/v) KOH. It was refluxed under N_2 atmosphere at 135–140 °C for 2 h (Abdeen 2005; Abdeen 2011; Abdeen 2015; Abdeen 2016; Abdeen et al. 2015; Abdeen and Mohammad 2014; Abdeen et al. 2013; Alsabagh et al. 2014). The deacetylated chitin (chitosan) was filtered, washed with distilled water, and dried (Fig. 1).

Preparation of CH/$Mg_{0.25}Co_{0.75}Fe_2O_4$ blending nanocomposite hydrogel

CH/$Mg_{0.25}Co_{0.75}Fe_2O_4$ nanocomposite in a mass ratio of 1:(0.01–0.1) was fabricated as follows: Chitosan (CH) has been

Fig. 1 The preparation of chitosan by deacetylation of chitin
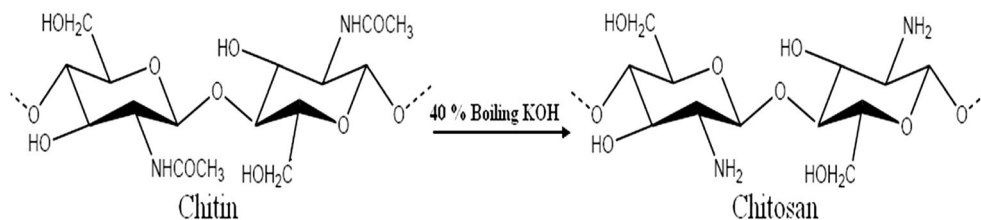
also dissolved in 2 wt% $C_2H_4O_2$ solution and the solid content in solution was 1.0 wt% and a certain amount of $Mg_{0.25}Co_{0.75}Fe_2O_4$ nanoparticles was dispersed into ethyl alcohol solution. Then, it was gradually dispersed into CH solution by ultrasonication for 30 min and stirred magnetically for more than 8 h. To this, 1.0 mol of epichlorohydrin was added under agitation. Finally, the resulting CH/$Mg_{0.25}Co_{0.75}Fe_2O_4$ smart nanocomposites were teemed into a circular glass template and were left stable at room temperature.

Treatment of oily wastewater by oil adsorption method and estimated of the crude oil residue by gravimetric method (Abdeen et al. 2015)

Crude oil of concentration (5.0 g/L) was placed in a series of 250-mL beakers containing 100 mL water. After adding a dose (0.1 g/L) of the prepared CH/$Mg_{0.25}Co_{0.75}Fe_2O_4$ nanocomposites into the suspension, and then leaving for a contact time of 1–24 h, maintaining pH value at 7 was reached for obtaining the best condition for elimination of the undesirable crude oil from the aqueous solution. The empirical proceedings were done at room temperature (30 ± 1 °C), and the mixtures have reached their high rapturous state using a mechanical shaker. The samples were taken off, and the oil removal portion was separated and calculated through removing the solvent by a rotary evaporator and weighed the resulting oil residue. The same previous steps were repeated using $Mg_{0.25}Co_{0.75}Fe_2O_4$ nanoparticles instead of CH/$Mg_{0.25}Co_{0.75}Fe_2O_4$ nanocomposites.

Characterizations

Nanocrystals and their unique and eco-friendly nanocomposites were examined using the step scan type GNR APD 2000 Pro X-ray diffractometer and CuKα1 radiation with $\lambda = 1.540598$ Å.

The lattice parameter a for cubic structure was calculated by (Cullity 1972)

$$a = d_{hkl}\left(h^2 + k^2 + l^2\right)^{1/2}$$

where (hkl) are miller indices and d_{hkl} is the inter-planer distance obtained by Bragg's law (Cullity 1972):

$$n\lambda = 2\,d_{hkl}\sin\theta$$

where n is the order of the reflection usually equal to one and θ is the Bragg's angle.

The acquired hopping lengths (the distances between the magnetic ions) at the A- and B-sublattices were calculated by using the following relations (Amer and El Hiti 2001, Amer et al. 2015):

$$L_A = a\frac{\sqrt{3}}{4} \quad \text{and} \quad L_B = a\frac{\sqrt{2}}{4}, respectively.$$

The elicited crystallite size (R) was determined using the higher intensity diffraction peak (311) and Sherrer's formula (Cullity 1978):

$$R = \frac{0.9\lambda}{\beta_{\frac{1}{2}}\cos\theta}$$

where $\beta_{\frac{1}{2}}$ is the full width at half maximum of the peak (311).

The calculated specific surface area S and the strain ε for the ultrafine particles were obtained using the following formulas (Amer et al. 2015):

$$\beta_{1/2}\cos\theta = \frac{0.9\lambda}{R} + 4\varepsilon\sin\theta \quad \text{and} \quad S = \frac{6000}{RD_x}$$

D_x is the deliberated X-ray density. The slope and the intercept of the straight line arising between $\beta_{1/2}\cos\theta$ and $4\sin\theta$ directly benefits in the exact evaluation of R and ε, respectively.

The derived unit cell volume V was elicited from the following expression (Yadav et al. 2016):

$$V\,(\text{Å}^3) = a^3$$

The determined experimental density D of the nanosamples was calculated by using the following relation (Safaan et al. 2006):

$$D = \frac{mass}{volume}\,(\text{gm/cm}^3)$$

where the mass of the samples was determined using an accurate digital balance (type OHAUS B 100) and the volume was calculated by measuring the sample dimensions.

The elicited theoretical density D_x (X-ray density) was calculated from the following relation:

$$D_x = \frac{ZM}{N_A V}\,(\text{gm/cm}^3)$$

where M is the molecular weight, Avogadro's number is $N_A = 6.023 \times 10^{23}$ molecules/mol, Z is the number of molecules per

unit cell which equals 8 for nanospinels structure, and V is the nanocrystal's unit cell volume (Yadav et al. 2016; Safaan et al. 2006).

The concluded porosity P value was obtained using the following formula (Amer et al. 2014):

$$P = 1 - \frac{D}{D_x}$$

where D and D_x are the experimental and theoretical (X-ray) densities, respectively.

IR spectra for all nanosamples were obtained by using Bruker Tensor 27 FT-IR Spectrometer in the range 200 to 4000 cm^{-1}, at room temperature. The force constant F_1 and F_2 for the A- and B-sites, respectively, are dependent on the bond length, Fe^{3+}–O^{2-}, and vibration frequency at these sites.

The force constant F_c was calculated by using the following equation (Amer et al. 2014):

$$F_c = 4\pi^2 C^2 \nu^2 \mu$$

where C is the velocity of light, ν is the sublattice vibration frequency, and μ is the reduced mass of Fe^{3+} and O^{2-} ions, equals about 2.061×10^{-23} g.

The magnetic nanoparticles were investigated with the JEOL JEM–100 SX transmission electron microscope (TEM); after exposing these nanomaterials to the ultrasonication for 45 min targeting the excellent separation of the nanoparticles from each other. Furthermore, the surface morphology of the hydrogel and their nanocomposites were investigated by the scanning electron microscope (JEOL JSM–6510 LV). Using sputtering technique, specimens were coated by an Au thin film; then, observation was carried out. Simultaneous thermo-gravimetric analysis (TGA) and differential thermal analysis (DTA) of the nanoferrite samples were carried out in N$_2$-atmosphere using a Perkin-Elmer STA 6000 thermal analysis system at heating rate of 15 °C/min.

Swelling degree

Swelling degree (D.S) was measured, where the pre-weighed dry sample was submerged in distilled H$_2$O for a specific time period. The excess adsorbed surface H$_2$O was isolated with absorptive paper, and the weight of turgid sample was carefully weighed. The previous proceedings were reiterated until no increase in the swollen sample final weight. D.S has been estimated using the following formula (Ferrus and Pages 1977):

$$DS = \left(m - m'\right)/m'$$

where the weights of swollen and dry samples are denoted by m and m', respectively.

Results and discussion

X-ray diffraction analysis

Figure 2(a) shows the X-ray diffraction (XRD) patterns of the as-prepared Mg$_{0.25}$Co$_{0.75}$Fe$_2$O$_4$ nanoparticles. The sharp and intensive arising reflection planes confirmed that these nanosamples have single-phase cubic spinel structure (Hankare et al. 2009; Darshane and Mulla 2010). The obtained value of the lattice constant a equals 8.41 Å and agrees well with the previous studies of spinel ferrites (Hankare et al. 2009; Darshane and Mulla 2010). The elicited crystallite size R value equals 25.02 nm, which reasonably lies in the nanoscale and resemble that obtained in the previously published work (Darshane and Mulla 2010). Principally, S gives significance and dependence on both the crystallite size R and X-ray density D_x, and ε relies on the crystallite size R. Since the nanoparticles have fine crystallite sizes, they have large specific surface areas (Dixit et al. 2012). S and ε values are indicated in Table 1. As well as the deduced values of the empirical density D and porosity P are indicated in Table 1, which matches well with the previously done literature (Amer et al. 2015). The acquired hopping length L_A and L_B values as well as unit cell volume V, the densities D_x, D, and porosity P are presented in Table 1.

Also, XRD patterns of the Mg$_{0.25}$Co$_{0.75}$Fe$_2$O$_4$/oil and CH/Mg$_{0.25}$Co$_{0.75}$Fe$_2$O$_4$/oil in Fig. 2(b, c) showed that the amorphous nature of chitosan is increasing and as a result, the crystallinity of Mg$_{0.25}$Co$_{0.75}$Fe$_2$O$_4$ nanostructures is decreasing, where amorphous diffraction peaks around $2\theta = 24°$ are indicating the intercalated Mg$_{0.25}$Co$_{0.75}$Fe$_2$O$_4$ into the chitosan matrix of the blending of CH/Mg$_{0.25}$Co$_{0.75}$Fe$_2$O$_4$ with adsorbed oil and also the disappearance of the sharp crystalline peaks related to Mg$_{0.25}$Co$_{0.75}$Fe$_2$O$_4$. Furthermore, Fig. 2(b) reveals that the oil does not result in the phase change of
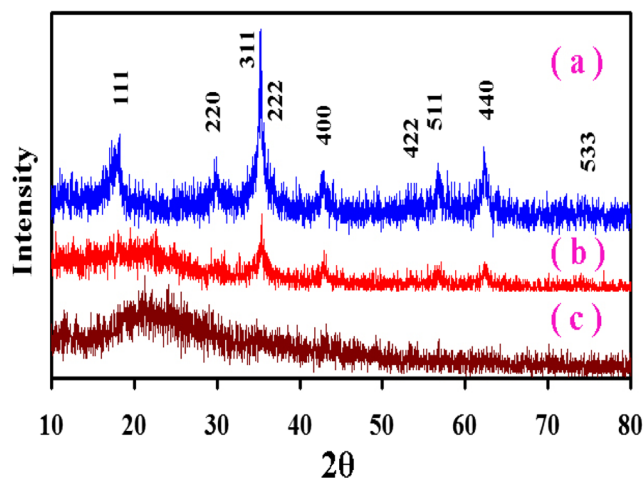
Fig. 2 XRD patterns for (a) the as-prepared Mg$_{0.25}$Co$_{0.75}$Fe$_2$O$_4$ nanoparticles, (b) Mg$_{0.25}$Co$_{0.75}$Fe$_2$O$_4$/ oil, and (c) CH/Mg$_{0.25}$Co$_{0.75}$Fe$_2$O$_4$/oil

Table 1 The obtained X-ray parameters, where a is the lattice constant, R is the crystallite size, L_A and L_B are the hopping lengths at A- and B-sites, S is the specific surface area, ε is the strain, D_x is X-ray density, D is the experimental density, P is the porosity, and V is the unit cell volume, respectively

Compound formula	a (Å)	R (nm)	L_A (Å)	L_B (Å)	S (m^2/g)	ε	D_x (gm/cm^3)	D (gm/cm^3)	P	V ($Å^3$)
$Mg_{0.25}Co_{0.75}Fe_2O_4$	8.41	25.02	3.640	2.97	47.74	-0.042	5.05	3.026	0.401	594.04

$Mg_{0.25}Co_{0.75}Fe_2O_4$ nanoparticles. Obviously, the use of a chitosan-based cross-linked network with the ferromagnetic $Mg_{0.25}Co_{0.75}Fe_2O_4$ nanoparticles induced an extreme widen of the emerged peaks (Fig. 2(c)), clearly indicating the occurrence of covalent cross-linking of the chitosan chains, with the consequent formation of chitosan Schiff bases. This augmentation of widening arises as a repercussion to the influence of amorphous and hybrid nature and structure of chitosan (Freire et al. 2016; de Lima et al. 2017). This elucidates the successful incorporation of the fine particles into the hydrogel polymer matrix. First, the $Mg_{0.25}Co_{0.75}Fe_2O_4$—H-O- interactions occur where chitosan is deposited onto the surface of the nanoparticles. Second, the $Mg_{0.25}Co_{0.75}Fe_2O_4$-chitosan nanocomposites are emerged from the effective and prosperous cross-linking of chitosan onto nanoparticle surfaces. Hydrogel nanocomposites were essentially formed by the polymerization of the magnetic $Mg_{0.25}Co_{0.75}Fe_2O_4$ nanoparticles to physically entrap the magnetic nanoparticles in the hydrogel matrix (Li et al. 2016; Abou Taleb 2014). The amorphous hump at $\sim 2\theta = 24°$ corresponding to the amorphous chitosan indicating the cross-linking, while this hump is missing from the chitosan free nanosamples (Freire et al. 2016).

FT-IR spectra

The FT-IR spectra are shown for the as-prepared spinel $Mg_{0.25}Co_{0.75}Fe_2O_4$ nanoparticles recorded in the range 200 to 4000 cm^{-1} in Fig. 3a. The results of IR are scheduled in Table 2. Where there are six bands for ν_1, ν_2, ν_4, ν_A, ν_B, and ν_T noticed in the spectra. The ν_1 at 582.5 cm^{-1} and ν_2 at 389.61 cm^{-1} assigned to the fundamental stretching vibrations of A-sites bonding, while the bigger retrieve strength for the bond-bending vibrations occur on B-sites (Cullity 1972). Ultimately, the confirmation of the evolution of the spinel structure is verified by the existence of both ν_1 and ν_2. It was plain that the values of ν_1 are shifted towards higher energies than that of ν_2. This is attributing to the decrease in bond lengths of the A-site clusters than that of the B-site clusters (Saafan et al. 2010). Also, it was observed the band at 244.95 cm^{-1} for ν_4 assigning to the lattice vibrations of the nanospinel system and it depends on the mass of each of the A-site divalent ions and their complexes, Fe^{2+}-O^{2-}, Co^{2+}-O^-, and/or Mg^{2+}-O^{2-} (Amer et al. 2014; Hashim et al. 2012). The triple band ν_T was emerged around 1568 cm^{-1} in IR spectra and was imputed to the existence of retained water

(humidity) in the samples (Saafan et al. 2010). The nonlinear molecule of water has three fundamental vibrational states: symmetric stretching, asymmetric stretching, and scissoring vibration modes (Saafan et al. 2010). The spectra around 850.59 and 1049.25 cm^{-1}, respectively, are relating to the bands ν_A and ν_B. The band ν_A may be related to the increase in the concentration of the divalent metallic ions Fe^{2+}, Mg^{2+}, and/or Co^{2+} among the A-sites. The band ν_B represents the tetravalent metal-oxygen vibrations and may be referring to the existence of the complexes Fe^{4+}-O^{2-}. Fe^{4+} cations refer to the electronic hopping between the Fe^{3+} and Fe^{2+} cations (Amer et al. 2014). In synchrony, both the split in ν_1 and Jahn-Teller effect of Fe^{2+} cations cause the existence of ν_A and ν_B bands (Amer et al. 2014).
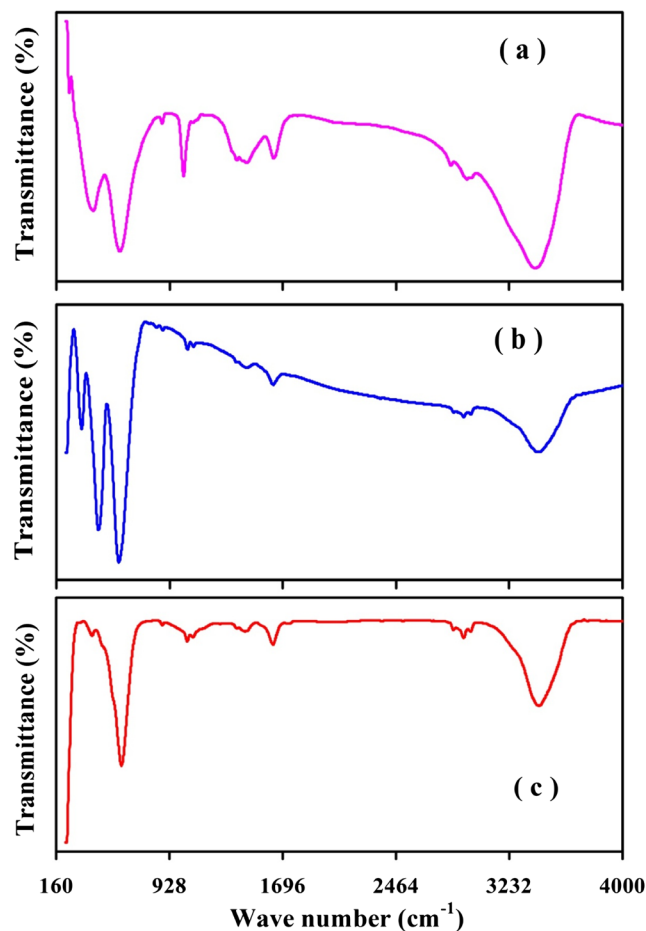
Fig. 3 FT-IR spectra of (**a**) the as-prepared $Mg_{0.25}Co_{0.75}Fe_2O_4$, (**b**) $Mg_{0.25}Co_{0.75}Fe_2O_4$/oil, and (**c**) CH/$Mg_{0.25}Co_{0.75}Fe_2O_4$/oil

Table 2 IR absorption band positions ν_n, n = 1, 2,…and B, threshold frequency ν_{Th}, Force constants F_1 and F_2 of A- and B-sites and Debye temperature θ_D, with error ± 0.3

Compound formula	ν_1 (cm⁻¹)	ν_2 (cm⁻¹)	ν_4 (cm⁻¹)	ν_A (cm⁻¹)	ν_B (cm⁻¹)	ν_{Th} (cm⁻¹)	F_1 (dyne/cm) × 10⁵	F_2 (dyne/cm) × 10⁵	θ_D (K)
Mg$_{0.25}$Co$_{0.75}$Fe$_2$O$_4$	582.5	389.61	244.95	866.02	1020.3	825.5	2.485	1.112	698.95

Debye temperature was obtained from the following equation (Patange et al. 2013a, b):

$$\theta_D = \frac{\hbar C \nu_{av}}{k} = 1.438\nu_{av} \quad \text{and} \quad \nu_{AV} = \frac{\nu_1 + \nu_2}{2}$$

where ν_{av} is the average value of wave numbers of bands, $\hbar = h/2\pi$, h is the Plank's constant, k is Boltzmann's constant, $C = 3 \times 10^{10}$ cm/s; C is the velocity of light and $\hbar C/k = 1.438$ for nanoferrite materials (Patange et al. 2013a, b): The value of θ_D equals 698.95 (K) and is affected by the wave number of IR bands (Patange et al. 2013a, b). Regarding the specific heat theorem; the elevation of the proportion of conduction electrons (n-type carriers) which basically acquire some of the heat energy decreasing its magnitude, and this reinforces the concept that conduction may be imputed to electrons, and vice versa. The threshold frequency ν_{th} existing at 771.5 cm⁻¹ for transition electrons can be deduced from the top point of the IR spectrum (Patange et al. 2013a, b): ν_{th} and θ_D are affected by the conduction electron numbers. The calculated values of force constants F_1 and F_2 for A- and B-sites, respectively, equals 2.485×10^5 and 1.112×10^5 dyne/cm which confirm the dependence of F_1 and F_2 on the vibration frequencies at these sites.

Figure 3b, c shows the infrared (IR) absorption spectra for as-prepared (AP) Mg$_{0.25}$Co$_{0.75}$Fe$_2$O$_4$ nanoparticles after adsorbed oil (Mg$_{0.25}$Co$_{0.75}$Fe$_2$O$_4$/oil) and their composites with chitosan after adsorbed oil (CH/Mg$_{0.25}$Co$_{0.75}$Fe$_2$O$_4$/oil) recorded in the range 200 to 4000 cm⁻¹. In comparison with spectra of the Mg$_{0.25}$Co$_{0.75}$Fe$_2$O$_4$ and Mg$_{0.25}$Co$_{0.75}$Fe$_2$O$_4$/oil, the stretching vibration peaks at around 2988 and 1109 cm⁻¹ in the spectra of CH/Mg$_{0.25}$Co$_{0.75}$Fe$_2$O$_4$/oil are for CH alkanes stretching and for (C–O–C) as a result of the formation of cross-linked network structures. Also, there are characteristic chitosan peaks around 1466 and 1636 cm⁻¹ of amino and amide groups of chitosan. It is Obvious that, these peaks characterizing chitosan are weak as a result for the presence of the chitosan in a small ratio (5%) with respect to Mg$_{0.25}$Co$_{0.75}$Fe$_2$O$_4$ (95%).

Elastic properties

For the as-prepared spinel Mg$_{0.25}$Co$_{0.75}$Fe$_2$O$_4$ nanoparticles, the obtained values of stiffness constants C_{11} and C_{12} (Table 3) were calculated using the following relations (Patange et al. 2013a, b):

$$C_{11} = \frac{F}{a} \quad \text{and} \quad C_{12} = \frac{C_{11}\sigma}{(1-\sigma)}$$

where F is the average force constant calculated by (El-Ghazzawy and Amer 2016; Amer et al. 2016); $F = (F_1 + F_2) / 2$ and σ is Poisson's ratio $[\sigma = 0.324(1–1.043p)]$, where P is the porosity (Patange et al. 2013a, b). The deduced value of σ is 0.094 (Table 3) which lies in the range from − 1 to 0.5 which is true according to the theory of isotropic elasticity. Force constant and type of bonding between Fe^{3+}, Mg^{2+}, and Co^{2+} cations within their crystalline structure as well has an impact on C_{11} and C_{12} (Patange et al. 2013a, b).

The distinguished moduli as Young's modulus E, bulk modulus K, and modulus of rigidity G are deduced from the following formulas (Patange et al. 2013a, b; Amer et al. 2016):

$$\text{Young's modulus} \quad E = \frac{(C_{11}-C_{12})(C_{11} + 2C_{12})}{(C_{11} + C_{12})}$$

$$\text{Rigidity modulus} \quad G = \frac{E}{2(\sigma + 1)}$$

$$\text{Bulk modulus} \quad K = \frac{1}{3}(C_{11} + 2C_{12})$$

Table 3 elucidates the three moduli (E, K, and G) for these nanomaterials. Their valuation greatly interprets the interatomic bonding strength as well as the degree of repulsion between Fe^{3+}, Mg^{2+}, and Co^{2+} cations and their prevalence within the nanocrystalline structure.

The persuasive evaluation for longitudinal elastic wave velocity (V_L), shear wave velocity (V_S), and the mean wave velocity (V_m) are deduced from the following formulations (Patange et al. 2013a, b; El-Ghazzawy and Amer 2016):

$$\text{Longitudinal velocity} \quad V_L = \left(\frac{C_{11}}{D_x}\right)^{\frac{1}{2}}$$

$$\text{Shear velocity} \quad V_S = \left(\frac{G_o}{D_x}\right)^{\frac{1}{2}}$$

The mean wave velocity V_m can be derived using the following relation: $\frac{3}{V_m^3} = \frac{1}{V_L^3} + \frac{2}{V_s^3}$ where G_o is the rigidity modulus with zero pore fraction. Table 3 exhibits the fine evaluation of V_L, V_S, and V_m. It is obvious that the direct effect and dependence of density D_x on both elastic moduli and wave velocities strongly affects their values (Patange et al. 2013a, b; El-Ghazzawy and Amer 2016).

Table 3 Stiffness constants, C_{11} and C_{12}, Young's modulus E, bulk modulus K, modulus of rigidity G, longitudinal elastic wave velocity (V_L), shear wave velocity (V_S), mean wave velocity (V_m), error ¼ ± 0.02, and absolute Poison ratio |σ|

Compound formula	C_{11} (GPa)	C_{12} (GPa)	E (GPa)	G (GPa)	K (GPa)	$V_L \times 10^3$ (m/s)	$V_S \times 10^3$ (m/s)	$V_m \times 10^3$ (m/s)	|σ|
$Mg_{0.25}Co_{0.75}Fe_2O_4$	213.9	22.2	209.73	95.86	86.1	6.508	3.757	4.17	0.094

Scanning electron microscope images

SEM micrograph was used to prove the adsorption of crude oil by the prepared materials (a) $Mg_{0.25}Co_{0.75}Fe_2O_4$/oil and (b) CH/$Mg_{0.25}Co_{0.75}Fe_2O_4$/oil samples as clear in Fig. 4. It appeared that the area of the most samples was coated with muddy-line substance of the oil adsorbed. As a result of coating the hydrogels with the oil molecules, the hydrogel (CH/$Mg_{0.25}Co_{0.75}Fe_2O_4$) surface appeared spreading and covering with muddy-line or rough surface having hollow-line pores (Fig. 4b). According to these clear micrographs, it was evidenced that the hydrogel adsorbed oil into its minute pores and an oily substance strata on the surface was developed. Figure 4b shows a layer with very clear and rough pores homogenously arranged. Moreover, the homopolymer resulting from binding of $Mg_{0.25}Co_{0.75}Fe_2O_4$ onto chitosan covered the surface. Though, a significant change of the structure and manifestation of the chitosan are shown in Fig. 4c. The considerable variation of the geometrical structure and semblance of chitosan possess a very clear and rough layer of pore structure; this is expected to have infiltrated adsorption and swelling properties. Also, Fig. 4 showed that the average grain size decreases nonlinearly for each composition. Whereas, the average grain size for the $Mg_{0.25}Co_{0.75}Fe_2O_4$/oil is 1.3 μm and for the CH/$Mg_{0.25}Co_{0.75}Fe_2O_4$ is 1.7 μm. It is obvious that the grain size is a bit bigger than the crystallite size determined by XRD which is due to the grain containing many crystallites and the new composite structure materials like petroleum oil and chitosan also increases the grain size (Prabhakaran et al. 2017; Kumar and Loganathan 2017; Gherca et al. 2013; Ismail et al. 2017; Noah et al. 2017).

Transmission electron microscope images

Typical images of the as-prepared (AP) $Mg_{0.25}Co_{0.75}Fe_2O_4$ nanoparticles are illustrated in Fig. 5. It is depicted that the nanoparticles are agglomerated which may point to the formation of ferromagnetically ordered nanoclusters. The obtained average nanoparticle size (Z) is 30.06 nm. It is clear that Z value is nearly similar to R value, where Z value is slightly larger. The comparatively larger Z values may refer to a superfine amorphous stratum on the nanoparticle surface. XRD can solely reveal the well-crystallite sections inside the nanoparticle, while TEM manifests over all illustration and picture of the nanoparticle (Prabhakaran et al. 2017; Kumar and Loganathan 2017).
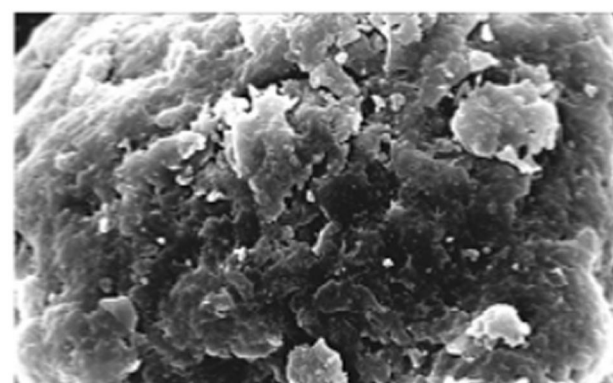
Thermal analysis (DTA/TGA)

DTA and TGA for the as-prepared $Mg_{0.25}Co_{0.75}Fe_2O_4$ spinel nanocrystals were implemented at changeable temperatures up to 1000 °C in N_2- ambience at a steady heating rate of 15 °C min^{-1}. Figure 6 elucidates the empirical DTA-TGA
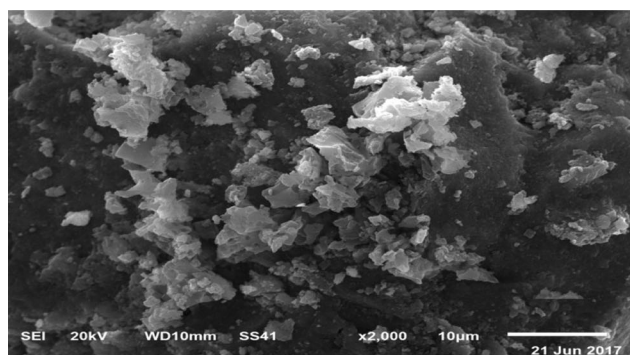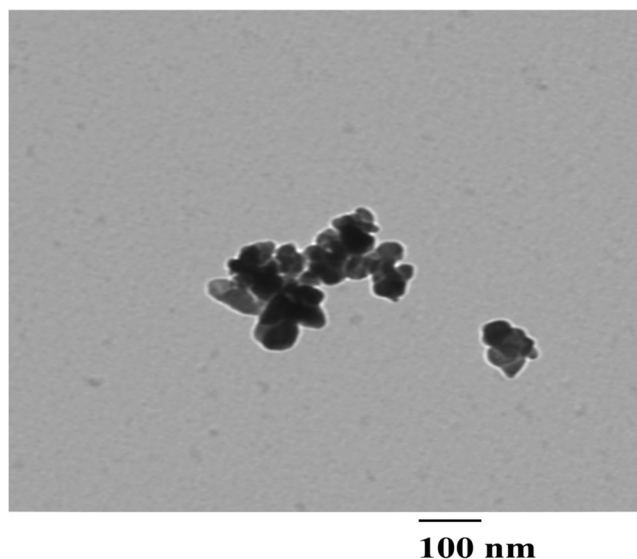

(a)
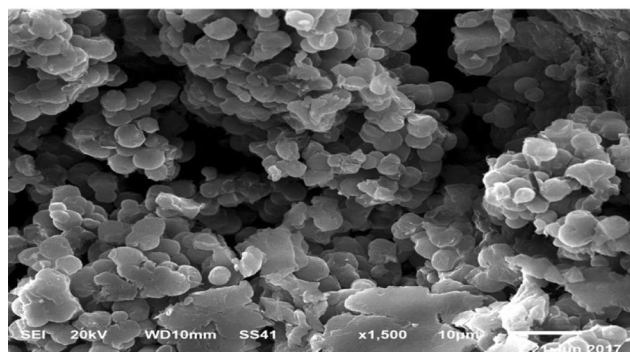
(b)

(c)

Fig. 4 SEM images of (**a**) $Mg_{0.25}Co_{0.75}Fe_2O_4$/oil, (**b**) CH/$Mg_{0.25}Co_{0.75}Fe_2O_4$/oil, and (**c**) CH

**Fig. 5** TEM images of the as-prepared (AP) spinel $Mg_{0.25}Co_{0.75}Fe_2O_4$ nanoparticles

Fig. 6 (**a**) DTA curve for the as-prepared spinel $Mg_{0.25}Co_{0.75}Fe_2O_4$ nanoparticles and (**b**) TGA curve for the as-prepared spinel $Mg_{0.25}Co_{0.75}Fe_2O_4$ nanoparticles

diagrams for these nanomaterials. The discerned weight forfeiture of ferrite nanoparticles eventuate in several distinct steps in the inspected temperature range which elaborate the evaporation of absorbed water molecules, formation of metal hydroxides, conversation of metal hydroxides into metal oxides and nanoferrite formation, respectively (Kumar and Loganathan 2017; Gherca et al. 2013; Ismail et al. 2017; Noah et al. 2017). The first small exothermic transition appears at ~ 47 °C and also the first small endothermic transformations appears at ~ 71 °C, where weight loss ranges in between 2.2 and 8.1% weight, which may be attributed to the volatilization of the residual water and dissociation of water molecules (Hankare et al. 2009; Ati et al. 2014). Obviously, for the fine particle size of these nanoparticles, a higher adsorption rate or water molecules occur on their surfaces (Ati et al. 2014). The earlier part of the combustion relation also shows other small exothermic transformation at ~ 100 °C, showing weight loss ~ 13.1% weight, which may be ascribed to the ongoing evaporation and dissociation of other residual water molecules (Hankare et al. 2009; Ati et al. 2014). According to this demeanor of the former junctures, this can be imputed to the dehydration of the nanosamples. The dehydration operation is accomplished at ~ 300 °C (Ati et al. 2014). The posterior weight forfeit happened in the temperature extent ranging from 250 to 350 °C is related to the decomposition and forming of metal hydroxide, revealing weight loss ~ 21–24.7% weight (Kumar and Loganathan 2017; Gherca et al. 2013; Ismail et al. 2017; Noah et al. 2017; Ati et al. 2014). Third weight loss arises from the transition of metal hydroxide into their corresponding metal oxide appears as an endothermic weight loss presented at 614 °C corresponding to weight loss 26% weight. The iron oxide (Fe_2O_3) is derived from iron hydroxide ($Fe_2(OH)_3$) and cobalt oxide (Co_3O_4) is from cobalt
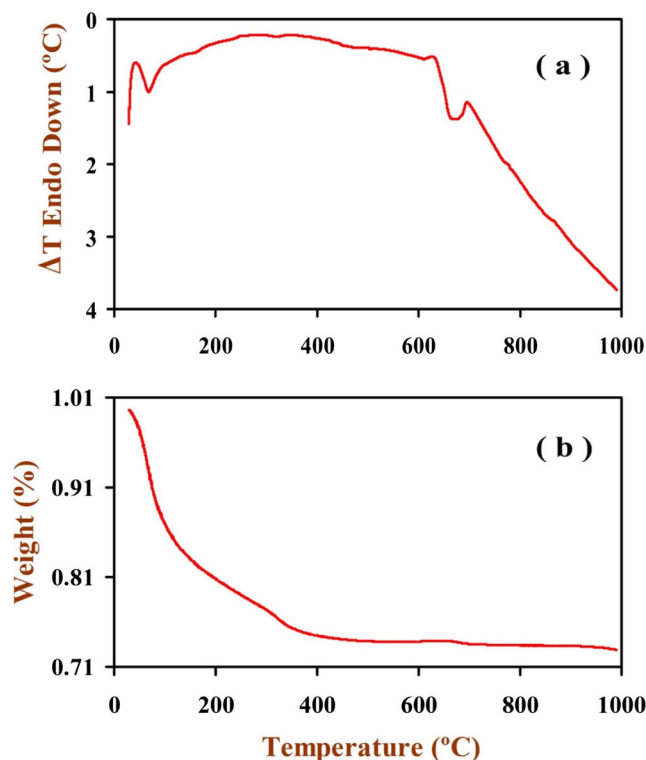
hydroxide ($Co(OH_2)$) at ~ 614 °C (Kumar and Loganathan 2017; Gherca et al. 2013; Ismail et al. 2017; Noah et al. 2017; Ati et al. 2014). The fourth weight loss giving endothermic peak and exothermic peak appeared at 620–675 °C and 700 °C are due to the decomposition of metal oxides and nucleation of stable nanoferrite phase ($Mg_{0.25}Co_{0.75}Fe_2O_4$ spinel nanoparticles), which shows a minimum weight loss 26.1–26.5% weight (Ati et al. 2014). DTA-TGA diagrams do not display a decrease in the weight after 750 °C. DTA-TGA curves elucidate an expansive exothermic peak up to ~ 700 °C which refer to the improvement of crystallization of the nanocrystals; the net weight loss of the samples heated from room temperature up to 1000 °C ranges in between 2.2 and 26.5% weight, where the extreme weight loss achieved at 100 °C and 614 °C. It is seen that the DTA pinnacles are absolutely corresponding to the weight forfeiture stages obtained from the TGA curve (Kumar and Loganathan 2017; Gherca et al. 2013; Ismail et al. 2017; Noah et al. 2017; Ati et al. 2014).

Swelling behavior

At various time intervals, the water uptake of CH/$Mg_{0.25}Co_{0.75}Fe_2O_4$ hydrogel was measured as shown in Fig. 7. These hydrogel samples showing a fast increase in water swelling to reach equilibrium with a high swelling
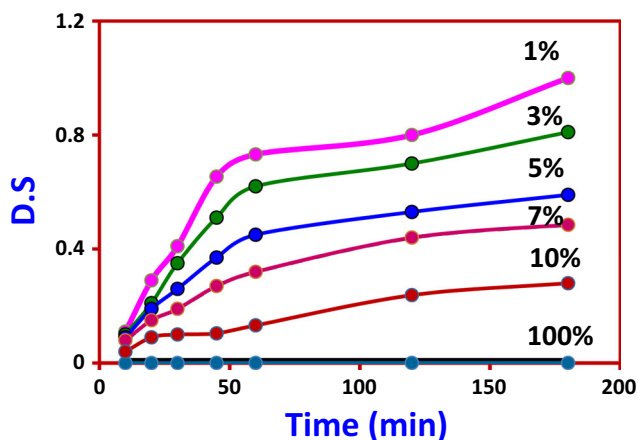
Fig. 7 Swelling degrees (D.S) of CH/$Mg_{0.25}Co_{0.75}Fe_2O_4$ hydrogels with different ratios of $Mg_{0.25}Co_{0.75}Fe_2O_4$ as a function of incubation time at pH = 7

Fig. 8 Removal percentage of crude oil in wastewater by different ratios of CH/$Mg_{0.25}Co_{0.75}Fe_2O_4$ hydrogels (95/5%, 0/100%) at pH 7 for 24 h

degrees range of 0.08–0.7, through 60 min. In this work, the CH/$Mg_{0.25}Co_{0.75}Fe_2O_4$ hydrogel with different ratios of the $Mg_{0.25}Co_{0.75}Fe_2O_4$ possesses an elevated swelling degree ranging from 0 to 1 degree; this may correspond to the surging of the free hydroxyl and amino functional groups capability of chitosan to establish hydrogen bonding with H_2O molecules. Blending CH hydrogel with $Mg_{0.25}Co_{0.75}Fe_2O_4$ will affect the numbers of the physical bonds of the OH and NH_2 groups with water molecules, with increasing$Mg_{0.25}Co_{0.75}Fe_2O_4$ fraction, so a higher proportion of H_2O binding sites will be formed. This makes more cross-linked network of hydrogel restricted the reaching and retained the water inside it. In this respect, the $Mg_{0.25}Co_{0.75}Fe_2O_4$ mingling with CH hydrogel was implemented to improve its adsorptive capacity for crude oil by increasing its binding sites.

Oil adsorption capacity of the CH/$Mg_{0.25}Co_{0.75}Fe_2O_4$ nanocomposites prepared

Owing to the needing to clean up the industrial by-products such as wastewater oil and/or oil/chemical spills/leaks, the elimination of crude oil from water has paying great attention among enormous academic and commercial interests. The hydrogels CH/$Mg_{0.25}Co_{0.75}Fe_2O_4$ nanocomposites can be best adsorbent material for getting rid of crude oil from oily wastewater, somewhere they were used to examine the performance of oil adsorption. Once a sample of hydrogel is placed in synthetic oily wastewater, the processes of adsorption and elimination started on the hydrogels surface and in the mixture of water/oil, respectively. The oil adsorption performance onto the prepared hydrogels and the elimination percentage at pH 7 by using different ratios of CH/$Mg_{0.25}Co_{0.75}Fe_2O_4$ hydrogels (95/5%, 0/100%) for equilibrium time 24 h were described in Fig. 8. It is clear that, the adsorption capability of the CH/$Mg_{0.25}Co_{0.75}Fe_2O_4$ nanocomposites for crude oil was designated by elimination percentage calculating that attained up to 72.56% and 50.2% respectively.
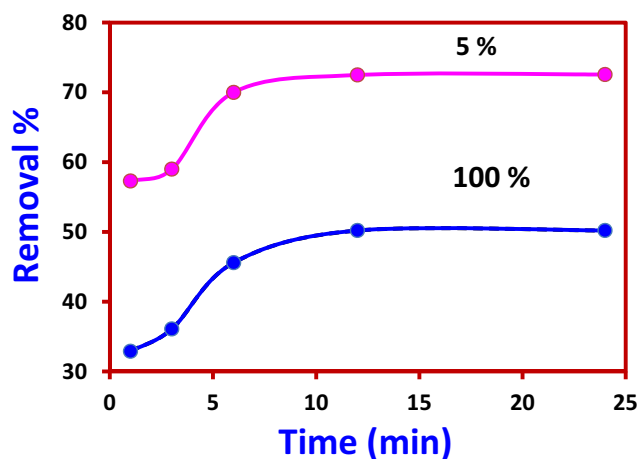
The brilliant oil adsorption ability demonstrated by the CH/$Mg_{0.25}Co_{0.75}Fe_2O_4$ nanocomposite gel (95/5%) may be referred to its extremely charge density of the chitosan as cationic polymer. The various adsorption abilities noticed among these adsorbents were attributed to the binding site numbers.

Conclusion

The $Mg_{0.25}Co_{0.75}Fe_2O_4$ and CH/$Mg_{0.25}Co_{0.75}Fe_2O_4$ hydrogels were prepared to produce nanoparticles and nanocomposite hydrogel respectively. The ability to adsorb the oil was studied for the $Mg_{0.25}Co_{0.75}Fe_2O_4$ and the best ratio of CH/$Mg_{0.25}Co_{0.75}Fe_2O_4$ nanocomposite hydrogel. The synthesized nanomaterials were characterized and it was found that the ratio $Mg_{0.25}Co_{0.75}Fe_2O_4$ in CH/$Mg_{0.25}Co_{0.75}Fe_2O_4$ has an effect on the water uptake of CH/$Mg_{0.25}Co_{0.75}Fe_2O_4$ nanocomposite hydrogel ability. Also, the ability of CH/$Mg_{0.25}Co_{0.75}Fe_2O_4$ to adsorb oil was optimum at 95/5%, at pH 7 and equilibrium time 24 h. The average nanoparticle size (Z) of $Mg_{0.25}Co_{0.75}Fe_2O_4$ was 30.06 nm. Also, XRD and SEM confirmed the fine size nature of $Mg_{0.25}Co_{0.75}Fe_2O_4$ nanostructures. As a result, the efficiency of the nanoferrites prepared for adsorption of crude oil from aqueous solution was improved by blending them with chitosan hydrogel (CH/$Mg_{0.25}Co_{0.75}Fe_2O_4$).

References

Abdeen Z (2005) Preparations and applications of some friendly environmental compounds. Ph.D. Thesis, Ain- Shams University, Cairo, Egypt, pp. 57

Abdeen Z (2011) Swelling and reswelling characteristics of cross-linked poly (vinyl alcohol) / chitosan hydrogel film. J Dispersion Sci Technol 32(9):1337–1344. https://doi.org/10.1080/01932691.2010.505869

Abdeen Z (2015) Encyclopedia of biomedical polymers and polymeric biomaterials. Taylor & Francis, Routledge

Abdeen Z (2016) Adsorption efficiency of poly(ethylene glycol)/chitosan/CNTblends for maltene fraction separation. Environ Sci Pollut Res 23:11240–11246. https://doi.org/10.1007/s11356-016-6225-0

Abdeen Z, Mohammad SG (2014) Study of the adsorption efficiency of an eco-friendly carbohydrate polymer for contaminated aqueous solution by organophosphorus pesticide. Open J. Organic Polym Mater 4:16–28. https://doi.org/10.4236/ojopm.2014.41004

Abdeen Z, Moustafa YMM (2015) Treatment of oily wastewater by using porous PVA hydrogels as oil adsorbent. J. Dispersion. Sci. Technol 37(2016 – Issue 6):799–805. https://doi.org/10.1080/01932691.2015.1062774

Abdeen Z, Attia HAE, Mohamad TGM (2013) Preparation, characterization and anti-fungal activity of biodegradable polymer (chitosan) on some Phytopathogenic fungi. J Appl Sci Res 1(1):60–71 www.scientiaresearchlibrary.com

Abdeen Z, Mohammad SG, Mahmoud MS (2015) Adsorption of Mn (II) ion on polyvinyl alcohol/chitosan dry blending from aqueous solution. Environ Nanotechnol Monit Manage 3:1–9. https://doi.org/10.1016/j.enmm.2014.10.001

Abdeen ZI, El Farargy AF, Negm NA (2017) Nanocomposite frame work of chitosan/polyvinyl alcohol / ZnO: preparation, characterization, swelling and antimicrobial evaluation. J Mol Liquids 250:335–343. https://doi.org/10.1016/j.molliq.2017.12.032

Abou Taleb MF (2014) Adsorption and photocatalytic degradation of 2-CP in wastewater onto CS/CoFe2O4 nanocomposite synthesized using gamma radiation. Carbohydr Polym 114:65–72. https://doi.org/10.1016/j.carbpol.2014.07.061

Akhtar MN, Sulong AB, Akhtar MN, Khan MA (2018) Systematic study of Ce^{3+} on the structural and magnetic properties of Cu nanosized ferrites for potential applications. J Rare Earths 36:156–164. https://doi.org/10.1016/j.jre.2017.09.003

Alsabagh AM, Elsabee MZ, Moustafa YM, Elfky A, Morsi RE (2014) Corrosion inhibition efficiency of some hydrophobically modified chitosan surfactants in relation to their surface active properties. Egypt J Pet 23(4):349–359. https://doi.org/10.1016/j.ejpe.2014.09.001

Amer MA, El Hiti M (2001) Mossbauer and X-ray studies for Ni.0.2ZnxMg0.8xFe2O4 ferrites. J Magn Magn Mater 234:118–125. https://doi.org/10.1016/S0304-8853(00)01406-2

Amer MA, Meaz TM, Attalah SS, Ghoneim AI (2014) Structural and magnetic characterization of the Mg0.2-xSrxMn0.8Fe2O4 nanoparticles. J Magn Magn Mater 363:60–65. https://doi.org/10.1016/j.jmmm.2014.03.067

Amer MA, Meaz TM, Hashhash A, Attalah SS, Ghoneim AI (2015) Structural properties and magnetic interactions in Sr-doped Mg-Mn nanoparticle ferrites. Mat Chem Phys 162:442–451. https://doi.org/10.1016/j.matchemphys.2015.06.013

Amer MA, Meaz TM, Attalah SS, Ghoneim AI (2016) Annealing effect on structural phase transition of as-synthesized Mg0.1Sr0.1Mn0.8Fe2O4 nanoparticles. J Alloys Compd 654:45–55. https://doi.org/10.1016/j.jallcom.2015.09.114

Ati AA, Othaman Z, Samavati A, Doust FY (2014) Structural and magnetic properties of Co–Al substituted Ni ferrites synthesized by co-precipitation method. J Mol Struct 1058:136–141. https://doi.org/10.1016/j.molstruc.2013.10.042

Attia EF, Zaki AH, El-Dek SI, Farghali AA (2017) Synthesis, physico-chemical properties and photocatalytic activity of nanosized Mg doped Mn ferrite. J Mol Liquids 231:589–596. https://doi.org/10.1016/j.molliq.2017.01.108

Cullity BD (1972) Introduction to magnetic materials. Addison-Wesley Publishing, Inc., Boston

Cullity B.D. (1978) Elements of X-ray diffraction, Second Edition, Addison-Wesley Publishing Company, INC, United States of America, Congress catalog No 56-10137

Darshane S, Mulla IS (2010) Influence of palladium on gas-sensing performance of magnesium ferrite nanoparticles. Mater Chem Phys 119:319–323. https://doi.org/10.1016/j.matchemphys.2009.09.004

de Lima LJ, Brito EL, da Silva RB, Franco RB Jr, da Costa JAP, de Vasconcelos CL, Soares JM (2017) Magnetic behavior in CoFe2-CoFe2O4 nanocomposites obtained from colloidal synthesis using chitosan and borohydride reduction. J. Magn. Magn. Mater. https://doi.org/10.1016/j.jmmm.2017.08.045

Dixit G, Singh JP, Srivastava RC, Agrawal HM (2012) Magnetic resonance study of Ce and Gd doped NiFe2O4 nanoparticles. J Magn Magn Mater 324:479–483. https://doi.org/10.1016/j.jmmm.2011.08.027

El-Ghazzawy EH, Amer MA (2016) Structural, elastic and magnetic studies of the as-synthesized Co1xSrxFe2O4 nanoparticles. J Alloys Compd 690:293–303. https://doi.org/10.1016/j.jallcom.2016.08.135

Ferrus R, Pages P (1977) Determination of the water retention value (WRV) of chitosan. Cellul Chem Technol 11:633

Freire TM, Dutra LMU, Queiroz DC, Ricardo NMPS, Barreto K, Denardin JC, Wurm FR, Sousa CP, Correia AN, de Lima-Neto P, Fechine PBA (2016) Fast ultrasound assisted synthesis of CHITOSAN-based magnetite NANOCOMPOSITES as a modified electrode sensor. Carbohydr Polym 151:760–769. https://doi.org/10.1016/j.carbpol.2016.05.095

Gherca D, Cornei N, Mentré O, Kabbour H, Daviero-Minaud S, Pui A (2013) In situ surface treatment of nanocrystalline MFe2O4 (M = Co, Mg, Mn, Ni) spinel ferrites using linseed oil. Appl Surf Sci 287:490–498. https://doi.org/10.1016/j.apsusc.2013.10.018

Goldman A (2006) Modern ferrite technology. Marcel Dekker Inc., New York ISBN 10: 0-387-29413-9 (e-book)

Hankare PP, Vader VT, Patil NM, Jadhav SD, Sankpal UB, Kadam MR, Chougule BK, Gajbhiye NS (2009) Synthesis, characterization and studies on magnetic and electrical properties of Mg ferrite with Cr substitution. Mater. Chem. Phys. 113:233–238. https://doi.org/10.1016/j.matchemphys.2008.07.066

Hashim M, Alimuddin KS, Shirsath SE, Kotnala RK, Chung H, Kumar R (2012) Structural properties and magnetic interactions in Ni0.5Mg0.5Fe2−xCrxO4 (0≤x≤1) ferrite nanoparticles. Powder Technol 229:37–44. https://doi.org/10.1016/j.powtec.2012.05.054

Ibrahim S, Wang S, Ang HM (2010) Removal of emulsified oil from oily wastewater using agricultural waste barley straw. Biochem Eng J 49:78–83. https://doi.org/10.1016/j.bej.2009.11.013

Inagaki M, Kawahara A, Nishi Y, Iwashita N (2002) Heavy oil sorption and recovery by using carbon fiber felts. Carbon 40:1487–1492. https://doi.org/10.1016/S0008-6223(01)00319-0

Ismail AS, Darwish MSA, Ismail EA (2017) Synthesis and characterization of hydrophilic chitosan-polyvinyl acetate blends and their sorption performance in binary methanol–water mixture. Egypt J Pet 26(1):17–22. https://doi.org/10.1016/j.ejpe.2016.02.006

Jagadeesha AV, Rudraswamy B, Sadhana K, Praveena K (2016) Structural and magnetic properties of manganese zinc ferrite nanoparticles prepared by solution combustion method using mixture of fuels. J Magn Magn Mater 409:111–115. https://doi.org/10.1016/j.jmmm.2016.02.096

Kasgöz H, Durmus A, Kasgöz A (2008) Enhanced swelling and adsorption properties of AAm-AMPSNa/clay hydrogel nanocomposites for heavy metal ion removal. Polym Adv Technol 19:213–220. https://doi.org/10.1002/pat.999

Kefeni KK, Mamba BB, Msagati TAM (2017) Application of spinel ferrite nanoparticles in water and wastewater treatment: a review.

Sep Purif Technol SEPPUR 13872:399–422. https://doi.org/10.1016/j.seppur.2017.07.015

Kumar K, Loganathan A (2017) The structural, electrical and magnetic properties of Co2+ content dependent Mg-Sr nanoferrite for electromagnetic induction. Mat Sci Eng B 224:48–55. https://doi.org/10.1016/j.mseb.2017.07.007

Li L, Zhang Z, Xie Y, Zhao J (2016) Preparation, characterization and magnetic properties of the BaFe12O19 @ chitosan composites. Solid State Sci 57:44–48. https://doi.org/10.1016/j.solidstatesciences.2016.05.003

Moazedh V (2005) Use of organo-clay/anthracite mixture in the separation of oil from oily waters. Energy Sources 27:101–112. https://doi.org/10.1080/00908310490448145

Noah AZ, El Semary MA, Youssef AM, El-Safty MA (2017) Enhancement of yield point at high pressure high temperature wells by using polymer nanocomposites based on ZnO & CaCO3 nanoparticles. Egypt J. Pet 26(1):33–40. https://doi.org/10.1016/j.ejpe.2016.03.002

Panpanit S, Visvanathan C (2001) The role of bentonite addition in UF flux enhancement mechanisms for oil/water emulsion. J Membr Sci 184:59–68. https://doi.org/10.1016/S0376-7388(00)00609-8

Paramesh D, Kumar KV, Reddy PV (2017) Effect of aluminium substitution on the electrical properties of Ni-Zn nanoferrites. J Magn Magn Mater 444:371–377. https://doi.org/10.1016/j.jmmm.2017.08.037

Patange SM, Shirsath SE, Lohar KS, Algude SG, Kamble SR, Kulkarni N, Mane DR, Jadhav KM (2013a) Infrared spectral and elastic moduli study of NiFe2xCrxO4 nanocrystalline ferrites. J Magn Magn Mater 325:107–111. https://doi.org/10.1016/j.jmmm.2012.08.022

Patange SM, Shirsath SE, Jadhav SP, Hogade VS, Kamble SR, Jadhav KM (2013b) Elastic properties of nanocrystalline aluminum substituted nickel ferrites prepared by co-precipitation method. J Mol Struct 1038:40–44. https://doi.org/10.1016/j.molstruc.2012.12.053

Prabhakaran T, Mangalaraja RV, Denardin JC, Jiménez JA (2017) The effect of reaction temperature on the structural and magnetic properties of nano CoFe2O4. Ceram. Intern 43:5599–5606. https://doi.org/10.1016/j.ceramint.2017.01.092

Saafan SA, Meaz TM, El-Ghazzawy EH, El Nimr MK, Ayad MM, Bakr M (2010) A.C. and D.C. conductivity of NiZn ferrite nanoparticles in wet and dry conditions. J Magn Magn Mater 322:2369–2374. https://doi.org/10.1016/j.jmmm.2010.02.039

Safaan SA, Abo El Ata AM, El Messeery MS (2006) Study of some structural and magnetic properties of Mn-substituted SrCu hexagonal ferrites. J Magn Magn Mater 302:362–367. https://doi.org/10.1016/j.jmmm.2005.09.041

Sharma VK, Mc Donald TJ, Kim H, Garg VK (2015) Magnetic graphene-carbon nanotube iron nanocomposites as adsorbents and antibacterial agents for water purification. Adv Colloid Interf Sci 225:229–240. https://doi.org/10.1016/j.cis.2015.10.006

Thakur A, Kumar P, Thakur P, Rana K, Chevalier A, Mattei J-L, Queffélec P (2016) Enhancement of magnetic properties of Ni0.5Zn0.5Fe2O4 nanoparticles prepared by the co-precipitation method. Ceram Int 42:10664–10670. https://doi.org/10.1016/j.ceramint.2016.03.173

Yadav RS, Havlica J, Masilko J, Kalina L, Wasserbauer J, Hajdúchová M, Enev V, Kuřitka I, Kožáková Z (2016) Impact of Nd^{3+} in CoFe$_2$O$_4$ spinel ferrite nanoparticles on cation distribution, structural and magnetic properties. J Magn Magn Mater 399:109–117. https://doi.org/10.1016/j.jmmm.2015.09.055